





Terahertz dielectric spectroscopy of human brain gliomas and intact tissues *ex vivo*: double-Debye and double-overdamped-oscillator models of dielectric response

A. A. GAVDUSH,^{1,10} N. V. CHERNOMYRDIN,^{1,2} G. A. KOMANDIN,¹ 
I. N. DOLGANOVA,^{2,3}  P. V. NIKITIN,⁴ G. R. MUSINA,¹ G. M.
KATYBA,³ A. S. KUCHERYAVENKO,^{1,3} I. V. RESHETOV,⁵ A. A.
POTAPOV,⁶ V. V. TUCHIN,^{7,8,9}  AND K. I. ZAYTSEV^{1,11} 

¹Prokhorov General Physics Institute of the Russian Academy of Sciences, Moscow, Russia

²Institute for Regenerative Medicine, Sechenov First Moscow State Medical University (Sechenov University), Moscow, Russia

³Institute of Solid State Physics of the Russian Academy of Sciences, Chernogolovka, Russia

⁴P.K. Anokhin Institute of Normal Physiology, Moscow, Russia

⁵Institute for Cluster Oncology, Sechenov First Moscow State Medical University (Sechenov University), Moscow, Russia

⁶Burdenko Neurosurgery Institute, Moscow, Russia

⁷Saratov State University, Saratov, Russia

⁸Institute of Precision Mechanics and Control of the Russian Academy of Sciences, Saratov, Russia

⁹National Research Tomsk State University, Tomsk, Russia

¹⁰arsenii.a.gavdush@gmail.com

¹¹kirzay@gmail.com

Abstract: Terahertz (THz) technology offers novel opportunities in the intraoperative neurodiagnosis. Recently, the significant progress was achieved in the study of brain gliomas and intact tissues, highlighting a potential for THz technology in the intraoperative delineation of tumor margins. However, a lack of physical models describing the THz dielectric permittivity of healthy and pathological brain tissues restrains the further progress in this field. In the present work, the *ex vivo* THz dielectric response of human brain tissues was analyzed using relaxation models of complex dielectric permittivity. Dielectric response of tissues was parametrized by a pair of the Debye relaxators and a pair of the overdamped-oscillators – namely, the double-Debye (DD) and double-overdamped-oscillator (DO) models. Both models accurately reproduce the experimental curves for the intact tissues and the WHO Grades I–IV gliomas. While the DD model is more common for THz biophotonics, the DO model is more physically rigorous, since it satisfies the sum rule. In this way, the DO model and the sum rule were, then, applied to estimate the content of water in intact tissues and gliomas *ex vivo*. The observed results agreed well with the earlier-reported data, justifying water as a main endogenous label of brain tumors in the THz range. The developed models can be used to describe completely the THz-wave – human brain tissues interactions in the frameworks of classical electrodynamics, being quite important for further research and developments in THz neurodiagnosis of tumors.

© 2020 Optical Society of America under the terms of the [OSA Open Access Publishing Agreement](#)

1. Introduction

Human brain gliomas are classified by the World Health Organization (WHO) into Grades I to IV [1]. They are among the most common and deadly pathologies of the brain, constituting ~ 26% of

all primary tumors and ~ 81% of primary malignant tumors of the brain [2]. Surgical resection of gliomas is the most common treatment strategy, while their gross total resection remains the most important prognostic factor that determines the patients' survival [3]. Unfortunately, intraoperative detection of gliomas might be challenging due to their unclear margins [4]. Nowadays, accurate delineation of glioma margins is provided only by the *ex vivo* histopathological examination of the excised tissue specimens using Hematoxylin and Eosin (H&E)-stained histology, aided by methods of molecular sensing and genetics [1]. Histopathological studies of tissues can be performed either intraoperatively (that significantly extend the terms of surgery) or post-operatively (aimed at confirming the preliminary diagnosis and the gross total resection). Despite histopathology still serves as a gold standard in diagnosis of the central nervous system tumors, there are increasing demands to the development of fast and accurate methods of intraoperative delineation of brain tumor margins.

Consider few widely-applied or just emerging modalities of brain tumor imaging. Among them, preoperative Magnetic Resonance Imaging (MRI) remains an irreplaceable instrument, applied for evaluating localization, dimensions, and margins of a tumor before surgery [5]. However, preoperative MRI data can be inaccurate for the intraoperative use due to the possible brain-shift. Alternatively, intraoperative MRI is translated to a clinical practice nowadays, being quite fast, accurate and effective [6,7]. At the same time, its integration into the modern neurosurgical workflows requires application of non-magnetic materials, and remains rather time-consuming and expensive. Another group of widespread intraoperative neuroimaging techniques is represented by fluorescent spectroscopy and imaging based on the 5-AminoLevulinic Acid (5-ALA) [8–10] or fluorescein sodium [11]. These methods are quite inexpensive and effective for the high-grade gliomas, but they show much lower efficiency for the low grades [12]. Such emerging modalities, as photoacoustic imaging [13], Raman spectroscopy and imaging [14,15], optical coherence tomography [16–18], visible and near-infrared spectroscopy [19], are vigorously explored, but still are far from clinical applications, being limited by one or more factors: brain-shift, use of contrast agents, limited sensitivity and specificity (especially, for low-grade gliomas), high labor intensity, etc. All these factors push further research and engineering efforts into realms of searching novel physical principles and imaging modalities, aimed at intraoperative diagnosis of brain tumors.

Among the emerging tools of the intraoperative neurodiagnosis, terahertz (THz) spectroscopy and imaging, which operate in the frequency range of ~ 0.1–3.0 THz (or the wavelength range of ~ 3 mm–100 μ m), attract increasing attention. Indeed, a rapid progress in THz technology [20–23] opens novel opportunities for the THz diagnosis of malignant and benign neoplasms with different nosologies and localizations [24,25]. THz waves are strongly absorbed by polar water molecules; thus, they are very sensitive to the content and state (free or bound) of water in tissues, which makes tissue water a main endogenous label of pathology at THz frequencies [24–26]. At the same time, such a strong absorption limits the depth of THz-wave penetration in tissues by few hundreds or even tens of microns depending on the tissue type and the considered frequency, thus, allowing one to probe only the superficial properties of tissues [24,25]. Given the larger THz wavelengths and the typical diffraction-limited spatial resolution of THz measurements on the order of few hundreds of microns (or even of few millimeters), the tissues are usually considered to be homogeneous at the scale posed by THz wavelengths [24,25,27]. This enables using the Rayleigh scattering theory, effective medium theory, and relaxation models of effective complex dielectric permittivity to describe the THz-wave – tissue interactions [24,25].

Most recently, an ability to use THz technology for the intraoperative diagnosis of brain tumors was studied, involving glioma models in mice and rats, as well as human brain gliomas featuring different WHO grades [28]. For example, in Ref. [29], orthotopic glioma model in rats was imaged in the THz range, where both freshly-excised and paraffin-embedded rat brain tissues *ex vivo* were considered. Differences between intact tissues and gliomas were observed in both cases.

For the freshly-excised tissues, they were attributed to the increased water content in a tumor due to the abnormal microvasculature, edema, and body fluids around necrotic debris. In turn, for the paraffin-embedded tissues, differences occurred owing to changes of cell density in a tumor. Furthermore, a contrast between the gray matter and the white matter was clearly observed, reportedly originating from higher content of myelin in the white matter [30]. In Ref. [31], paraffin-embedded intact tissues and glioma model (GL261 cell line) from mice were studied *ex vivo* using THz pulsed spectroscopy. The observed results justified a contrast between intact and tumorous tissues in paraffin blocks and revealed some optimal spectral bands and features for the differentiation between healthy and pathological tissues. In Ref. [32], intact tissues and glioma model (C6 cell line) from rats were studied using THz pulsed spectroscopy. By analyzing complex refractive index of tissues, the authors estimated the increased water content in a tumor and claimed it as the main factor underlying a contrast between intact and tumorous tissues. In Refs. [33–35], a potential of THz reflectometry and imaging in the intraoperative neurodiagnosis was highlighted involving *ex vivo* and *in vivo* glioma models (eGFP+GSC-11, C6, and U87-MG cell lines) from mice and rats, as well as few *ex vivo* high-grade gliomas of the human brain.

Despite the aforementioned favorable results of the *ex vivo* and *in vivo* THz measurements of glioma models, the latter only partially mimic biophysical properties of human brain tumors, while their THz dielectric response can differ in a large extent. Therefore, in our previous works [36,37], we applied THz pulsed spectroscopy to study *ex vivo* the optical properties of gelatin-embedded intact tissues and WHO Grades I–IV gliomas of the human brain, where gelatin embedding allowed us to preserve tissues from hydration/dehydration and, thus, to sustain their THz response unaltered as compared to the freshly-excised ones [38]. From Fig. 1, we noticed statistical differences between the THz response of intact tissues and gliomas of all WHO grades, while the response of edematous tissue was close to that of a tumor. Evidently, edema (along with traumatic brain injuries [39,40]) can be confused with a tumor, thus, complicating delineation of its margins.

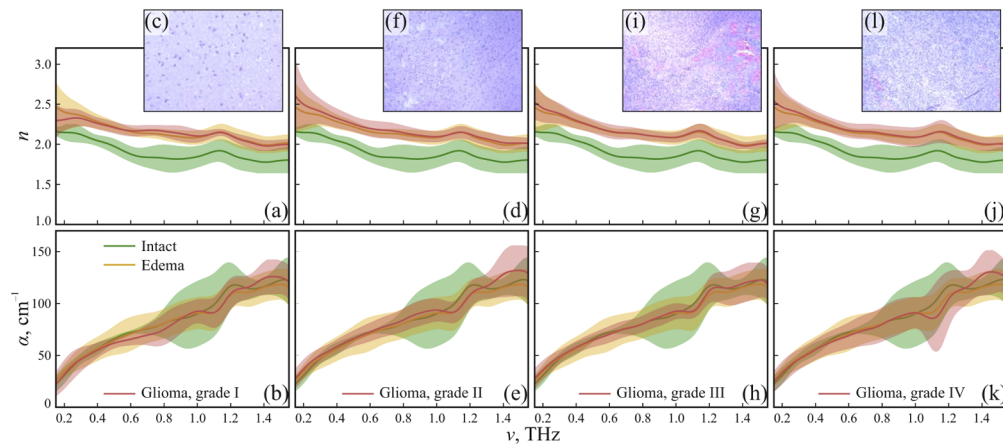


Fig. 1. *Ex vivo* refractive index n , absorption coefficient α (by field), and H&E-stained histology of gelatin-embedded human brain gliomas of the different WHO Grades: (a)–(c) Grade I; (d)–(f) Grade II; (g)–(i) Grade III; (j)–(l) Grade IV. The THz optical properties of gliomas are compared with equal data for the intact and edematous tissues, while the error bars represent a $\pm 2.0\sigma$ confidential interval of measurements. Reprinted from an open access Ref. [36] published by SPIE Press under a CC BY license.

In spite of such a rapid progress in THz diagnosis of gliomas, there is still a lack of physical models describing dielectric permittivity of healthy and pathological human brain tissues in the THz range. In order to mitigate this problem, in this work, we analyze the *ex vivo* THz

complex dielectric permittivity of intact tissues and WHO Grade I–IV gliomas using two distinct models – namely, the double-Debye (DD) model, based on a pair of the Debye relaxators, and the double-overdamped-oscillator (DO) model, based on a pair of the Lorentz oscillators with a high damping constant. We demonstrate a simple mathematical relation between these models. Both models are shown to accurately reproduce experimental data for the intact tissues and gliomas. While the DD model is more usual in THz biophotonics, the DO model is more physically rigorous, satisfying the sum rule. Therefore, in this work, the DO model and the sum rule are applied to estimate the content of water in human brain tissues. The observed results agree with the earlier-reported data, justifying water as a main endogenous label of brain tumors in the THz range. Thus developed models of THz dielectric response of human brain tissues could bring significant contribution to further research and engineering efforts in the THz intraoperative neurodiagnosis.

2. THz pulsed spectroscopy of human brain tissues *ex vivo*

In this work, we consider the same set of 26 human brain glioma samples *ex vivo*, which was used in our previous paper [36]. It comprised of 2, 9, 4, and 11 samples of glioma tissue featuring WHO Grades I to IV, respectively. After resection in the Burdenko Neurosurgery Institute (Moscow, Russia), the tissue specimens were fixed by gelatin slabs for further characterization using THz pulsed spectroscopy in the frequency range of 0.2–1.5 THz. Gelatin embedding of tissues allowed to sustain hydration and, thus, THz response of tissues *ex vivo* unaltered (as compared to those of freshly-excised tissues *ex vivo*) during transportation and THz measurements [38].

For tissue characterization, a homemade THz pulsed spectrometer was used, the detailed description of which is given in Refs. [37,41]. It is equipped with a housing for the THz beam path purging with nitrogen gas, which yields suppression of a water vapors' impact on the measured data. At the same time, the measured sample is handled atop of the flat crystalline quartz window at an ambient room atmosphere, while the window serves simultaneously as a sample holder and as a spacer between the nitrogen gas and an ambient atmosphere. The applied spectrometer operates in reflection mode and uses a pair of gold-coated off-axis parabolic mirrors in order to focus the THz beam on the "crystalline-quartz – tissue" interface and to collimate the reflected part of the THz beam. Detailed description of this experimental setup and outline of the mathematical procedures applied for reconstruction of the tissue THz optical properties can be found in Ref. [36].

After the spectroscopic measurements, the tissue samples were fixed in formalin and transferred to the Burdenko Neurosurgery Institute for further routine histopathological examination, which involves, in particular, H&E-stained histology; see Fig. 1. It is worth noting that, along with the WHO Grade I–IV gliomas, we analyzed perifocal tissues, which often surround a tumor and are comprised of intact (healthy) and edematous tissues with the distinct THz response, as evident from Fig. 1.

Thus reconstructed optical properties of intact tissues, edema, and WHO Grade I–IV gliomas of the human brain are shown in Fig. 1. These data form a basis for our analysis of picosecond relaxation dynamics in tissues involving methods of dielectric spectroscopy. For this aim, it is convenient to represent the THz spectroscopy data in form of a complex dielectric permittivity $\tilde{\epsilon}$ defined as

$$\tilde{\epsilon} = \epsilon' - i\epsilon'' \quad (1)$$

where ϵ' and ϵ'' are its real and imaginary parts, respectively. It is related to the complex refractive index \tilde{n} , or the refractive index n and absorption coefficient α (by field) as

$$\tilde{n} = n' - in'' \equiv n - i\frac{c_0}{2\pi\nu}\alpha \equiv \sqrt{\tilde{\epsilon}}, \quad (2)$$

where, $n' \equiv n$ and n'' stand for its real and imaginary parts, correspondingly, $c_0 \approx 3 \times 10^8$ m/s is the speed of light in free space, ν is an electromagnetic-wave frequency.

3. Relaxation models of tissue dielectric response in the THz range

In our analysis, two distinct models of complex dielectric permittivity, which account for the picosecond relaxation dynamics of tissue water, are considered.

First one is the DD model, which is comprised of the two Debye relaxation terms and widely exploited in THz biophotonics [24,25,42,43]

$$\tilde{\varepsilon} = \varepsilon_{\infty} + \frac{\Delta\varepsilon_1}{1 + i\omega\tau_1} + \frac{\Delta\varepsilon_2}{1 + i\omega\tau_2}, \quad (3)$$

where $\omega = 2\pi\nu$ is an angular frequency, $\Delta\varepsilon_1$, $\Delta\varepsilon_2$ are magnitudes that regulate a contribution of "slow" and "fast" Debye relaxations with the time constants τ_1 , τ_2 to the tissue dielectric response, while ε_{∞} is a constant dielectric permittivity at high-frequencies (compared to the analyzed spectral range, $\nu \gg (2\pi\tau_{1,2})^{-1}$). This model is quite convenient and yields accurate parametrization of the THz spectroscopic data for water, water solutions, biological liquids and tissues; only 5 independent coefficients are required for this aim – ε_{∞} , $\Delta\varepsilon_1$, $\Delta\varepsilon_2$, τ_1 , and τ_2 . In Fig. 2, the DD model is shown for the dielectric response of liquid water with the parameters $\varepsilon_{\infty} = 4.1$, $\Delta\varepsilon_1 = 72.2$, $\Delta\varepsilon_2 = 2.5$, $\tau_1 = 10.6$ ps, and $\tau_2 = 0.18$ ps. reported in Ref. [42]. This DD model describes two broad absorption bands in ε'' -curve, which are attributed to the "slow" and "fast" relaxations of water and centered at the inverse relaxation times of $(2\pi\tau_1)^{-1}$, $(2\pi\tau_2)^{-1}$. In turn, ε' -curve tends to decrease with increasing frequency featuring the high-frequency magnitude ε_{∞} and the low-frequency magnitude $\varepsilon_{\infty} + \Delta\varepsilon_1 + \Delta\varepsilon_2$.

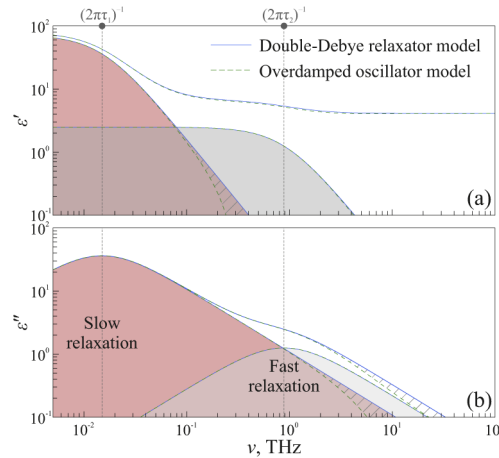


Fig. 2. A comparison of the DD (Eq. (3)) and DO (Eq. (4)) models of complex dielectric permittivity $\tilde{\varepsilon}$ for a liquid water: (a),(b) real ε' and imaginary ε'' parts of $\tilde{\varepsilon}$, respectively. The DD model is plotted based on the parameters from Ref. [42], while the DO model is calculated via Eq. (5).

Second, we consider the well-known in condensed matter physics DO model [44,45], which is comprised of two Lorentz terms with a high damping constant

$$\tilde{\varepsilon} = \varepsilon_{\infty} + \frac{\Delta\varepsilon_1}{1 - \frac{\omega^2}{\omega_{01}^2} + i\frac{\omega\gamma_1}{\omega_{01}^2}} + \frac{\Delta\varepsilon_2}{1 - \frac{\omega^2}{\omega_{02}^2} + i\frac{\omega\gamma_2}{\omega_{02}^2}}, \quad (4)$$

where $\Delta\varepsilon_1$, $\Delta\varepsilon_2$, ω_{01} , ω_{02} , and γ_1 , γ_2 stand for magnitudes, quasi-resonant frequencies (given by the restoring forces) and damping constants, respectively, of the "slow" and "fast" relaxation

processes, that are equivalent to the "slow" and "fast" Debye relaxations in Eq. (3). It is worth noting that a constant ε_∞ and magnitudes of each i -th Debye relaxation term $\Delta\varepsilon_i$ are equal to that of a corresponding overdamped oscillator. Other parameters of the i -th overdamped oscillator can be easily and univocally calculated based on parameters of the corresponding Debye relaxation term by resolving the following equations:

$$\gamma_i = \omega_{0,i}^2 \tau_i, \quad \gamma_i = C \omega_{0,i}, \quad C \gg 1. \quad (5)$$

Given that the inequality $C \gg 1$ is satisfied, particular value of constant C is not so important. For example, in this work, we assumed this parameter to be as large as $C = 10^2$. In the overdamped oscillator, parameters $\omega_{0,i}$, γ_i lose their separate physical meaning, and only their combination $\omega_{0,i}/\gamma_i = \tau_i^{-1}$ defines maximum in the loss spectrum – i.e. in the ε'' -curve [44]. In Fig. 2, the DO model is calculated for water using Eq. (5) based on the abovementioned parameters of the DD model from Ref. [42]. It should be noticed that the overdamped oscillators reproduce the shape of dielectric permittivity curves ε' , ε'' .

From Fig. 2, it is clear that both the Debye kernel and the overdamped oscillator are practically equivalent at low-frequencies up to $\omega \sim (2\pi\tau_i)^{-1} < \omega_{0,i} \ll \gamma_i$; but for $\omega > (2\pi\tau_i)^{-1}$, the Debye model predicts higher losses than those of the overdamped oscillator [44]. Unlike the overdamped oscillator, the Debye kernel does not fulfill the sum rule for the oscillator strengths and, thus, predicts infinite number of charge carriers / dipoles N underlying the dielectric response of a medium [44,46,47]

$$N \propto \int_0^\infty \omega \varepsilon'' d\omega = \text{finite}. \quad (6)$$

In turn, integration of the conductivity given by the i -th overdamped-oscillator term results in a finite value $\Delta\varepsilon_i \omega_{0,i}^2 = \Delta\varepsilon_i \gamma_i^2 / C^2$, where $\omega_{0,i}^2 = N_i q_i^2 / m_i \varepsilon_0$; N_i is the number of dipoles contributing to the i^{th} relaxation process, while q_i and m_i are effective charge and mass of each dipole. Therefore, for the high-frequency range and for the estimation of a number of charges/dipoles in a medium, the overdamped oscillator model is preferable, being more physically rigorous than the Debye or related models, such as the Cole-Cole [48,49], Davidson-Cole [50], or Havriliak-Negami [51]. Such an advantage of the overdamped oscillator over the Debye relaxator makes it more appropriate for THz biophotonics.

4. Modeling complex dielectric permittivity of human brain tissues *ex vivo*

The described DD and DO models of dielectric permittivity were applied for fitting the results of the *ex vivo* THz pulsed spectroscopy of intact tissues and WHO Grade I–IV gliomas of the human brain, which are reprinted in Fig. 1.

For this aim, the THz responses of all tissues were recalculated in form of the real ε' and imaginary ε'' parts of the complex dielectric permittivity $\tilde{\varepsilon}$ (Eqs. (1), 2). Then, parameters of the DD model were calculated by fitting of the experimental data with Eq. (3), for which we exploited the weighted least-square method in MATLAB software. For all considered tissue types, we set the time constants of "slow" and "fast" relaxation processes τ_1 , τ_2 to be equal to that of water from Ref. [42], which reduced the problem dimensionality and simplified the fitting procedure, providing appropriate model parameters. It should be noticed that the experimental results of each THz measurement for each considered sample were fitted by the DD model independently, which, then, allowed us to calculate both mean values and standard deviations of the calculated model parameters. Finally, parameters of the DO model (Eq. (4)) were calculated based on those of the DD one via Eq. (5).

In Fig. 3, we illustrate the experimental ε' , ε'' -curves, which are overlapped with the DD and DO models of complex dielectric permittivity, as well as compared with the DD model of liquid water from Ref. [42]. It is clear from these results that these two models appear to be equal in

the considered spectral range, accurately reproducing the experimental data and accommodating the experimental error bars. As expected, both ε' - and ε'' -curves of tissues response are below those of a liquid water, but feature quite similar frequency-dependent character.

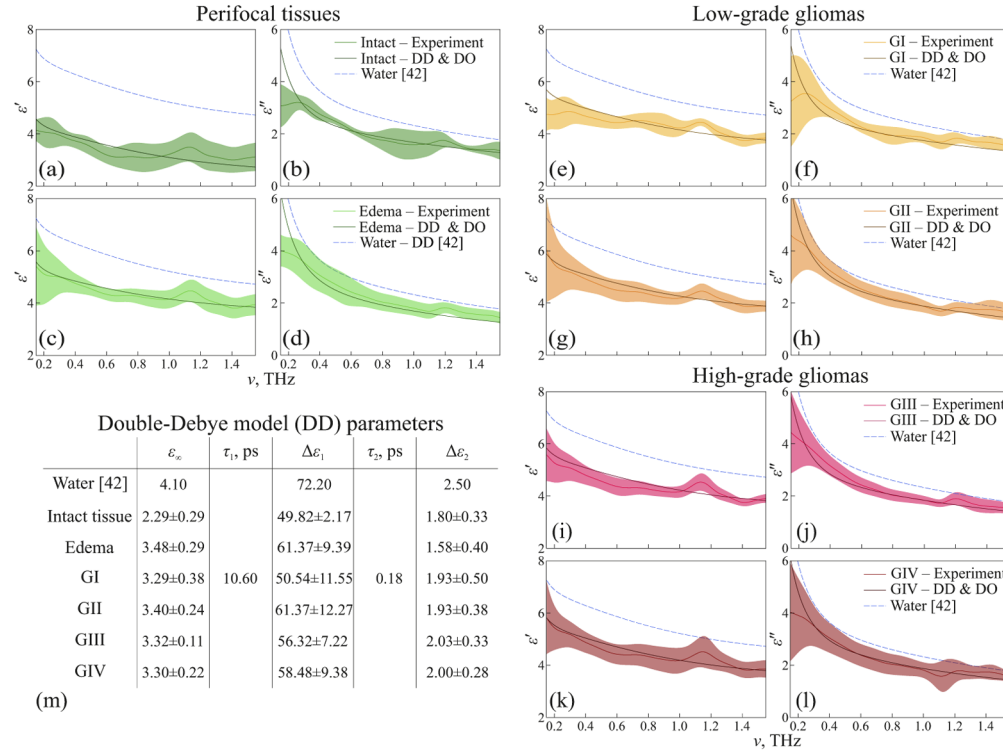


Fig. 3. *Ex vivo* THz complex dielectric permittivity $\tilde{\varepsilon}$ of the intact tissues, edematous tissues and gliomas of the human brain: (a),(b) measured real ε' and imaginary ε'' dielectric permittivity parts for the intact brain tissues, as compared with the DD (Eq. (3)) and DO (Eq. (4)) models; (c)–(l) the same data for the edematous tissues and gliomas; (m) the DD model parameters for water and tissues, from which parameters of the DO model can be calculated using Eq. (5). In (a)–(l), dielectric properties of tissues are compared with the DD model of liquid water from Ref. [42]. Here, GI–GIV stands for the WHO Grade I–IV gliomas.

Here, one can notice that slightly larger error bars are observed for the intact tissues as compared to those of the edema and gliomas, which can be attributed to the unaccounted difference between the THz optical properties of white matter and gray matter. Indeed, due to small amount of intact tissues studied in Ref. [36], we did not differentiate these two types of intact tissues during measurements of perifocal regions of a tumor. At the same time, white matter and gray matter possess distinct response at THz frequencies due to (predominantly) the different content of myelin [29,30].

The dielectric parameters ε_∞ , $\Delta\varepsilon_1$, $\Delta\varepsilon_2$, which are equal for the DD and DO models, are presented in Fig. 4 for all considered groups of human brain tissues. From panel (a), it is evident that ε_∞ is higher for the edematous tissues and gliomas of all grades, as compared to that of the intact tissues. This difference can be attributed to the increase water content and the increased cell density in edematous tissue and a tumor [29,52,53]. The increased magnitudes of both "slow" and "fast" relaxations $\Delta\varepsilon_1$, $\Delta\varepsilon_2$ for all tumor grades, observed from Fig. 4, might be attributed to the higher content of polar H₂O molecules in such tissues [26]. At the same time, dielectric

parameters ε_∞ , $\Delta\varepsilon_1$, $\Delta\varepsilon_2$ are smaller for tissues than for water, as expected, since water content is limited by $f < 100\%$.

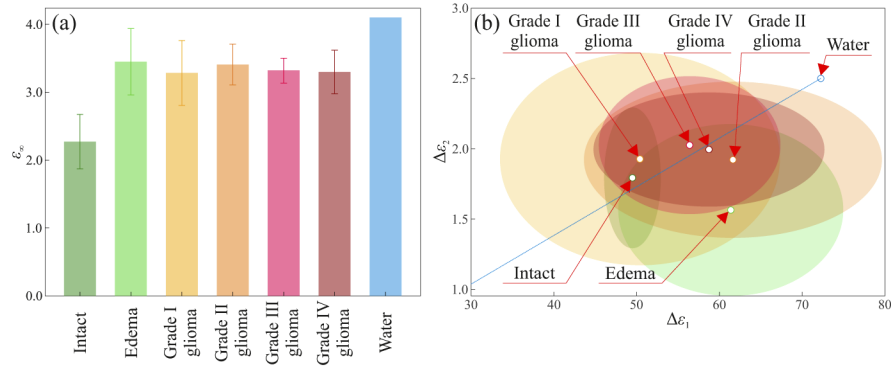


Fig. 4. Dielectric parameters ε_∞ , $\Delta\varepsilon_1$, $\Delta\varepsilon_2$ for the intact tissues, edema and gliomas, which are equal for the DD and DO models: (a) dielectric constant at high frequencies ε_∞ ; (b) magnitudes of the "fast" and "slow" relaxation processes $\Delta\varepsilon_1$, $\Delta\varepsilon_2$. The error bars in (a) and the colored areas in (b) represent $\pm 3\sigma$ confidential intervals. The data is compared with the DD model of liquid water from Ref. [42]. Here, GI–GIV stand for the WHO Grades I–IV gliomas. In (b), we show a blue line, at which a ratio between the two relaxation terms $\Delta\varepsilon_1/\Delta\varepsilon_2$ is constant and equal to that of a liquid water.

Different magnitudes of the two relaxation processes $\Delta\varepsilon_1$, $\Delta\varepsilon_2$, observed in Fig. 4 for the liquid water and tissues can be analyzed from the viewpoint of water bonding and segregation. As demonstrated in Ref. [54], dielectric constants (ε_∞ , $\Delta\varepsilon_1$, $\Delta\varepsilon_2$) are much smaller for bound water than for free. Furthermore, "slow" relaxation term of bound water ($\Delta\varepsilon_1$) appears to be suppressed much stronger than that of the "fast" one ($\Delta\varepsilon_2$), which reducing the ratio $\Delta\varepsilon_1/\Delta\varepsilon_2$, as compared to a liquid water. In turn, segregation can change dynamics of water molecules and, thus, a ratio $\Delta\varepsilon_1/\Delta\varepsilon_2$ in a complex and less-predictable manner [55]. When liquid water interacts with a medium without any pronounced changes in its dynamics, we can expect it to appear on a blue line in Fig. 4(b), which define a constant ratio $\Delta\varepsilon_1/\Delta\varepsilon_2$ equal to that of a liquid water. For the WHO Grade IV gliomas, this ratio is similar to a liquid water, which might be attributed to a large amount of free water in such tissue due to necrotic debris. This ratio is smaller for the intact tissues and WHO Grade I, III gliomas, which might point out water bonding. Finally, an increased ratio is inherent to the WHO Grade II gliomas and edema, which is difficult to quantify at this time, and more investigations are in order. One should notice that THz spectroscopy seems to be sub-optimal for the analysis of tissues water bonding and segregation owing to very broadband absorption peaks given by the "fast" and "slow" relaxations; see Fig. 1. More physically-reasonable analysis of water dynamics in healthy and pathological tissues, aided by different instruments (for example, infrared Fourier spectroscopy [45], backward-wave oscillator spectroscopy [56], and Raman spectroscopy [57]), seems to be prospective for addressing this challenge.

It is worth noting that dielectric parameters ε_∞ , $\Delta\varepsilon_1$, $\Delta\varepsilon_2$ can serve as physically-reasonable principle components for the differentiation between healthy and pathological human brain tissues, when using THz pulsed spectroscopy as an intraoperative diagnosis tool, as suggested in Ref. [58] for the THz diagnosis of basal cell carcinoma of the skin. However, we postponed a detailed analysis of such an opportunity to our future studies.

5. Estimation of water content in tissues

Water content in tissues f can be approximately estimated involving the sum rule

$$f = \frac{N_{\text{tissue}}}{N_{\text{water}}} \equiv \frac{\int_{\omega_{\min}}^{\omega_{\max}} \omega \varepsilon''_{\text{tissue}} d\omega}{\int_{\omega_{\min}}^{\omega_{\max}} \omega \varepsilon''_{\text{water}} d\omega}, \quad (7)$$

where integration of imaginary part ε'' of the complex dielectric permittivity within the considered spectral range of ω_{\min} to ω_{\max} is involved for tissues, in the numerator, and for a liquid water, in the denominator. In our opinion, such an estimation relies on the first principles and, thus, forms a favorable alternative to the simplified linear spectral decomposition technique [25], the method proposed by Yamaguchi et al. [32], or others [59]. As we would show below, it yields quite physically reasonable data, agreeing well with other considerations.

In Fig. 5(a), the calculated water content f is shown for the intact tissues, edema, and WHO Grade I–IV gliomas *ex vivo*. We observed the water content of $71.1 \pm 6.8\%$ in intact tissues, while that in edema and all glioma Grades is ~ 5 – 10% higher. WHO Grade II–IV gliomas show the highest content of water, while for the WHO Grade IV gliomas it can be as large as $80.6 \pm 8.6\%$. In Fig. 5(a), we also notice quite large error bars, which are given by fluctuations of the dielectric permittivity model parameters over the considered set of tissue specimens; they are attributed to the native variability of endogenous optical properties of tissues [60,61]. Other possible reason of such variability originates from uncertainties of the experimental data fitting by the two broad absorption bands given by Eqs. (3) and (4), which are centered slightly above (or at the edges) of the spectral operation range of THz pulsed spectrometer (see Figs. 1, 2) [24].

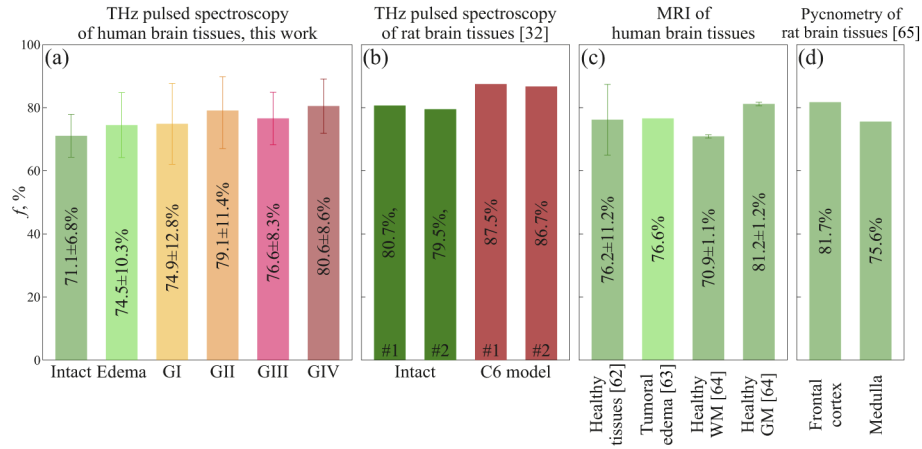


Fig. 5. Water content in healthy and pathological tissues of the brain measured using different experimental techniques: (a) intact tissues, edema, and WHO Grade I–IV gliomas of the human brain *ex vivo* measured by the THz pulsed spectroscopy in this work; (b) intact tissues and C6 glioma model from rat brain *ex vivo* measured by the THz pulsed spectroscopy in Ref. [32]; (c) healthy human brain tissues and tumoral edema *in vivo* measured by MRI in Refs. [62–64], where WM and GM stand for white matter and gray matter, respectively; (d) healthy rat brain tissues *ex vivo* measured by a pycnometer in Ref. [65]. Here, error bars represent fluctuations of water content within the considered set of tissue specimens.

Thus estimated water content in human brain tissues can be compared with few well-known studies, which were based on different experimental techniques. In Fig. 5(b), we show water content in freshly-excised intact tissues and C6 glioma model from the rat brain *ex vivo*, estimated from the THz pulsed spectroscopy data by Yamaguchi and co-authors [32]. Despite they revealed

slightly higher average water content in both intact tissues and glioma model, the observed difference between them is quite similar to our estimations, thus, demonstrating $\sim 5\text{--}10\%$ higher water content in tumors. Such a variance between the results of the two compared studies can be due to both different methods applied for water content estimation based on processing of the THz pulsed spectroscopy signals and (possibly) distinct water content, which changes the THz response of human and rat brain tissues (both healthy and pathological).

Next, in Fig. 5(c), we consider water content in healthy brain tissues (including white matter and gray matter) and tumoral edema of the human brain studied by MRI in Refs. [62,64]. These MRI-based estimations demonstrate that our data is quite reasonable. The MRI data on water content in tumoral edema from Ref. [63] appeared to be very close to that in intact tissues from Ref. [62], which appears to be surprising and even illogical; thus, we attribute this effect to possible differences of methods and signal processing routine applied in these two MRI-based studies. Estimations from Ref. [64] demonstrate that water content in white and gray matters statistically varies, which should lead to distinct response of such tissues in the THz ranges; thus, this effect should be accounted in our future studies.

Finally, by means of the results from Ref. [65], we consider estimation of water content in healthy rat brain tissues using pycnometry. This technique relies on a completely different physical principle of water content estimation, but shows quite similar results as compared to our data; thus, additionally justifying its reasonability.

6. Discussion

As mentioned above, the developed DD and DO models of complex dielectric permittivity (see Eqs. (3)–5 along with Fig. 3), allow us to describe the THz-wave interactions with both intact tissues and WHO Grade I–IV gliomas of the human brain *ex vivo*. In particular, this provides an ability to:

- model the THz-wave interaction with layered media using a plane-wave approximation along with the Fresnel equations (for describing the THz-wave transmission and reflection at interfaces between media), and the modified Bouguer–Lambert–Beer law (for describing the THz-wave phase shifts and absorption in a bulk medium); such modeling is of great importance in THz spectroscopy of tissues [24,25];
- simulate numerically the THz-wave interaction with biological objects of a complex shape using methods of computational electrodynamics or statistical Monte-Carlo approaches; such modeling is of high importance for the correct understanding of THz radiation transport in biological tissues [24,25];
- apply parameters of the DD or DO models as physically-reasonable principal components for the discrimination between different tissue types [58].

Therefore, the developed models can be quite useful for further research and engineering efforts in THz biophotonics, in general, and THz neurodiagnosis of tumors, in particular.

It is worth noting that the two analyzed relaxation bands, that underlie the dielectric response of water and tissues in the GHz–THz range (see Fig. 2), are centered beyond or at the edges of the considered spectral range of our THz pulsed spectrometer. This can lead to some inaccuracies of the experimental data parametrization by the dielectric permittivity models. Evidently, method of broadband dielectric measurements, which combines backward-wave oscillator spectroscopy, THz pulsed spectroscopy, Fourier-transform infrared spectroscopy and other techniques [45,56], can help to obtain much accurate data about the picosecond relaxation dynamics of liquid water and tissues. Despite attractiveness of such broadband measurements, they still remain quite a daunting task due to technical difficulties and time constraints of tissue measurements using the above-mentioned instruments. Therefore, in our study, we used only the THz pulsed

spectroscopy with its quite broad spectral operation range and technical flexibility, while we postponed broadband measurements to our future studies.

Real biological systems might possess more complex dielectric response in the THz range. Particularly, its dielectric permittivity model can be comprised of three or even more relaxation terms, each of which represents a particular fraction of free/bound or segregated water, with its distinct electrodynamic characteristics [54,55]. In general, dielectric response of such media can obey more complex regularities, involving integration of the relaxation process kernel over a continuous spectrum of the relaxation states; for example, for the Debye relaxation kernel, such integral response has the form [44,66,67]

$$\tilde{\varepsilon} = \varepsilon_{\infty} + \int_0^{\infty} \frac{g(\tau)}{1 + i\omega\tau} d\tau, \quad (8)$$

where $g(\tau)$ is a continuous relaxation-time spectrum. Overall, we still have quite limited understanding of relations between the complex molecular dynamics of liquid and tissue water [68] and its broadband electrodynamic response. Nevertheless, the detailed analysis of such complex dielectric permittivity models and of underlying physical mechanisms is a topic of further comprehensive research work. Such models can be overabundant for the considered broadband relaxation electrodipole excitations of matter, while the considered DD and DO models provide quite accurate description of biological tissue response in most cases [24,25].

All data presented in this paper were obtained and analyzed relying on an assumption of homogeneous tissue character at the scale posed by the THz wavelengths, which is typical for the THz biophotonics [24,36]. This assumption allows for using the effective medium theory and parametrizing the experimental data by different dielectric permittivity models. However, an increasing number of research papers demonstrates scattering properties of tissues in the THz range. For example, in Ref. [69], the authors shown that the cross-polarization THz imaging provides some contrast for the tumor margins delineation, while such polarization changes cannot be predicted in the framework of the effective medium theory. Furthermore, our latest results on the THz solid immersion microscopy [27,70,71] reveal structural inhomogeneities of different biological tissues *ex vivo*, that can become the origin of the Mie scattering effects. For the considered intact tissues and gliomas of the human brain, structural heterogeneity can occur thanks to the different optical properties of healthy white and gray matters [30], the neurovascular structural elements of the brain, the presence of necrotic debris in the WHO Grade IV gliomas [18], or other factors. Nevertheless, such a heterogeneous character of human brain tissues still have not been studied in the THz range, and it deserves further comprehensive research work.

The described methods for estimation of water content in biological tissues relying on the THz pulsed spectroscopy signal processing and the sum rule holds strong potential in THz biophotonics, where water plays a role of endogenous label of pathological processes in most cases [24,25]. At the same time, estimation of the water content in tissues based on THz data might be carried using alternative approaches. Among them is the simplified linear spectral decomposition technique used in earlier studies. Otherwise, number of water dipoles in system can be calculated by analytical integration of the sample dynamic conductivity predicted by the DO model. However, for this aim, one should know effective masses and charges of dipoles, that contribute to the different relaxation processes and that cannot be estimated based on the THz data. Therefore, in this paper, we used simplified numerical integration of the sample dynamic conductivity within the spectral operation range of our spectrometer. This method resulted in quite reasonable predictions of water content in tissues, which agreed well with the earlier-reported data; thus, justifying correctness of our considerations.

7. Conclusion

In this study, we analyzed the THz complex dielectric permittivity of the *ex vivo* intact tissues and WHO grade I–IV gliomas of the human brain using the DD and DO models. It is worth noting that the obtained results are consistent with the previously-reported data, which involved measurements of both glioma models from rats and mice, and few tumors of the human brain [28–37]. Human brain tumors and edematous tissues feature higher refractive index and absorption coefficient in the THz range that correlates well with the previously-reported differences between intact tissues and tumors of the brain, that were represented in form of the THz time-domain waveforms or tissue reflectivity. It was demonstrated that both models accurately reproduce our spectroscopic measurements of brain tissues in the THz range. We show that the DO model is more physically rigorous, since it satisfies the sum rule. Estimation of water content in tissues relying on the THz pulsed spectroscopy data yields the results that are in agreement with the earlier-reported measurements involving different experimental techniques, which justifies water as a main endogenous label of brain tumors at THz frequencies. Thus developed DD and DO models yield description of THz-wave — human brain tissues interactions, being quite useful for further research and engineering efforts in the area of THz neurodiagnosis.

Funding

Russian Science Foundation (18–12–00328); Ministry of Science and Higher Education of the Russian Federation (075–15–2020–790).

Acknowledgments

Development of relaxation models, that describe the THz dielectric response of human brain tissues, by G.A. Komandin, P.V. Nikitin, G.R. Musina, G.M. Katyba, A.S. Kucheryavenko was supported by the Russian Science Foundation (RSF), Project # 18–12–00328. The work of N.V. Chernomyrdin and K.I. Zaytsev on analysis of different factors, which underlie the tissue response at THz frequencies, was supported by the Ministry of Science and Higher Education of the Russian Federation, Project # 075–15–2020–790.

Disclosures

The authors declare no conflict of interest.

References

1. D. Louis, A. Perry, G. Reifenberger, A. von Deimling, D. Figarella-Branger, W. Cavenee, H. Ohgaki, P. Wiestler, O. D. Kleihues, and D. Ellison, “The 2016 world health organization classification of tumors of the central nervous system: a summary,” *Acta Neuropathol.* **131**(6), 803–820 (2016).
2. Q. Ostrom, G. Cioffi, H. Gittleman, N. Patil, K. Waite, C. Kruchko, and J. Barnholtz-Sloan, “CBTRUS statistical report: Primary brain and other central nervous system tumors diagnosed in the United States in 2012–2016,” *Neuro Oncol.* **21**(Supplement_5), v1–v100 (2019).
3. E. Chang, A. Clark, R. Jensen, M. Bernstein, A. Guha, G. Carrabba, D. Mukhopadhyay, W. Kim, L. Liao, S. Chang, J. Smith, M. Berger, and M. McDermott, “Multiinstitutional validation of the University of California at San Francisco Low-Grade Glioma Prognostic Scoring System,” *J. Neurosurg.* **111**(2), 203–210 (2009).
4. M. Hefti, H. Mehdorn, I. Albert, and L. Dorner, “Fluorescence-guided surgery for malignant glioma: A review on aminolevulinic acid induced protoporphyrin IX photodynamic diagnostic in brain tumors,” *Curr. Med. Imaging Rev.* **6**(4), 254–258 (2010).
5. C. Nimsy, O. Ganslandt, P. Hastreiter, R. Wang, T. Benner, A. Sorensen, and R. Fahlbusch, “Preoperative and intraoperative diffusion tensor imaging-based fiber tracking in glioma surgery,” *Neuro Surg.* **56**(1), 130–138 (2005).
6. P. Willems, J. van der Sprenkel, C. Tulleken, M. Viergever, and M. A. Taphoorn, “Neuronavigation and surgery of intracerebral tumours,” *J. Neurol.* **253**(9), 1123–1136 (2006).
7. C. Senft, A. Bink, K. Franz, H. Vatter, T. Gasser, and V. Seifert, “Intraoperative mri guidance and extent of resection in glioma surgery: a randomised, controlled trial,” *Lancet Oncol.* **12**(11), 997–1003 (2011).

8. S. Goryaynov, G. Widhalm, M. Goldberg, D. Chelushkin, A. Spallone, K. Chernyshov, M. Ryzhova, G. Pavlova, A. Revischin, L. Shishkina, V. Jukov, T. Savelieva, V. Loschenov, and A. Potapov, "The role of 5-ala in low-grade gliomas and the influence of antiepileptic drugs on intraoperative fluorescence," *Front. Oncol.* **9**, 423 (2019).
9. B. Schatlo, J. Fandino, N. Smoll, O. Wetzel, L. Remonda, S. Marbacher, W. Perrig, H. Landolt, and A.-R. Fathi, "Outcomes after combined use of intraoperative MRI and 5-aminolevulinic acid in high-grade glioma surgery," *Neuro Oncol.* **17**(12), 1560–1567 (2015).
10. S. Goryaynov, A. Batalov, N. Zakharova, I. Pronin, A. Baev, E. Pogosebkyan, L. Fadeeva, D. Chelushkin, and A. Potapov, "Fluorescence diagnosis with 5 ALA and noncontrast ASL-perfusion in the planning of brain gliomas surgery," *Neuro Oncol.* **20**(suppl_3), iii230 (2018).
11. B. Chen, H. Wang, P. Ge, J. Zhao, W. Li, H. Gu, G. Wang, Y. Luo, and D. Chen, "Gross total resection of glioma with the intraoperative fluorescence-guidance of fluorescein sodium," *Int. J. Med. Sci.* **9**(8), 708–714 (2012).
12. N. Pustogarov, D. Pantelev, S. Goryaynov, A. Ryabova, E. Rybalkina, A. Revischin, A. Potapov, and G. Pavlova, "Hiding in the shadows: Cpx expression and 5-ala induced fluorescence in human glioma cells," *Mol. Neurobiol.* **54**(7), 5699–5708 (2017).
13. M. Kircher, A. de la Zerda, J. Jokerst, C. Zavaleta, P. Kempen, E. Mittra, K. Pitter, R. Huang, C. Campos, F. Habte, R. Sinclair, C. Brennan, I. Mellinghoff, E. Holland, and S. Gambhir, "A brain tumor molecular imaging strategy using a new triple-modality MRI-photoacoustic-Raman nanoparticle," *Nat. Med.* **18**(5), 829–834 (2012).
14. D. Orringer, B. Pandian, Y. Niknafs, T. Hollon, J. Boyle, S. Lewis, M. Garrard, S. Hervey-Jumper, H. Garton, C. Maher, J. Heth, O. Sagher, D. Wilkinson, M. Snuderl, S. Veneti, S. Ramkissoon, K. McFadden, A. Fisher-Hubbard, A. Lieberman, T. Johnson, X. Xie, J. Trautman, C. Freudiger, and S. Camelo-Piragua, "Rapid intraoperative histology of unprocessed surgical specimens via fibre-laser-based stimulated raman scattering microscopy," *Nat. Biomed. Eng.* **1**(2), 0027 (2017).
15. M. Jermyn, J. Desroches, J. Mercier, K. St-Arnaud, M.-C. Guiot, F. Leblond, and K. Petrecca, "Raman spectroscopy detects distant invasive brain cancer cells centimeters beyond mri capability in humans," *Biomed. Opt. Express* **7**(12), 5129–5137 (2016).
16. K. Yashin, E. Kiseleva, E. Gubarkova, A. Moiseev, S. Kuznetsov, P. Shilyagin, G. Gelikonov, I. Medyanik, L. Kravets, A. Potapov, E. Zagaynova, and N. Gladkova, "Cross-polarization optical coherence tomography for brain tumor imaging," *Front. Oncol.* **9**, 201 (2019).
17. E. Kiseleva, K. Yashin, A. Moiseev, L. Timofeeva, V. Kudelkina, A. Alekseeva, S. Meshkova, A. Polozova, G. Gelikonov, E. Zagaynova, and N. Gladkova, "Optical coefficients as tools for increasing the optical coherence tomography contrast for normal brain visualization and glioblastoma detection," *Neurophotonics* **6**(03), 1 (2019).
18. I. Dolganova, P. Aleksandrova, P. Nikitin, A. Alekseeva, N. Chernomyrdin, G. Musina, S.-I. Beshplav, I. Reshetov, A. Potapov, V. Kurlov, V. Tuchin, and K. Zaytsev, "Capability of physically reasonable OCT-based differentiation between intact brain tissues, human brain gliomas of different WHO grades, and glioma model 101.8 from rats," *Biomed. Opt. Express* **11**(11), 6780–6798 (2020).
19. E. Genina, A. Bashkatov, D. Tuchina, P. Dyachenko (Timoshina), N. Navolokin, A. Shirokov, A. Khorovodov, A. Terskov, M. Klimova, A. Mamedova, I. Blokhina, I. Agranovich, E. Zinchenko, O. Semyachkina-Glushkovskaya, and V. Tuchin, "Optical properties of brain tissues at the different stages of glioma development in rats: pilot study," *Biomed. Opt. Express* **10**(10), 5182–5197 (2019).
20. H. Guerboukha, K. Nallappan, and M. Skorobogatii, "Toward real-time terahertz imaging," *Adv. Opt. Photonics* **10**(4), 843–938 (2018).
21. A. Yachmenev, D. Lavrukhin, I. Glinskiy, N. Zenchenko, Y. Goncharov, I. Spektor, R. Khabibullin, T. Otsuji, and D. Ponomarev, "Metallic and dielectric metasurfaces in photoconductive terahertz devices: a review," *Opt. Eng.* **59**(06), 1 (2019).
22. A. Yachmenev, S. Pushkarev, R. Reznik, R. Khabibullin, and D. Ponomarev, "Arsenides-and related III-V materials-based multilayered structures for terahertz applications: Various designs and growth technology," *Prog. Cryst. Growth Charact. Mater.* **66**(2), 100485 (2020).
23. K. Zaytsev, G. Katyba, N. Chernomyrdin, I. Dolganova, A. Kucheryavenko, A. Rossolenko, V. Tuchin, V. Kurlov, and M. Skorobogatii, "Overcoming the abbe diffraction limit using a bundle of metal-coated high-refractive-index sapphire optical fibers," *Adv. Opt. Mater.* **8**(18), 2000307 (2020).
24. K. Zaytsev, I. Dolganova, N. Chernomyrdin, G. Katyba, A. Gavdush, O. Cherkasova, G. Komandin, M. Shchedrina, A. Khodan, D. Ponomarev, I. Reshetov, V. Karasik, M. Skorobogatii, V. Kurlov, and V. Tuchin, "The progress and perspectives of terahertz technology for diagnosis of neoplasms: a review," *J. Opt.* **22**(1), 013001 (2020).
25. O. Smolyanskaya, N. Chernomyrdin, A. Konovko, K. Zaytsev, I. Ozheredov, O. Cherkasova, M. Nazarov, J.-P. Guillet, S. Kozlov, Y. Kistenev, J.-L. Coutaz, P. Mounaix, V. Vaks, J.-H. Son, H. Cheon, V. Wallace, Y. Feldman, I. Popov, A. Yaroslavsky, A. Shkurinov, and V. Tuchin, "Terahertz biophotonics as a tool for studies of dielectric and spectral properties of biological tissues and liquids," *Prog. Quantum Electron.* **62**, 1–77 (2018).
26. G. McIntyre, "Cell hydration as the primary factor in carcinogenesis: A unifying concept," *Med. Hypotheses* **66**(3), 518–526 (2006).
27. N. Chernomyrdin, V. Zhelnov, A. Kucheryavenko, I. Dolganova, G. Katyba, V. Karasik, I. Reshetov, and K. Zaytsev, "Numerical analysis and experimental study of terahertz solid immersion microscopy," *Opt. Eng.* **59**(06), 061605 (2019).

28. G. Musina, P. Nikitin, N. Chernomyrdin, I. Dolganova, A. Gavdush, G. Komandin, D. Ponomarev, A. Potapov, I. Reshetov, V. Tuchin, and K. Zaytsev, "Prospects of terahertz technology in diagnosis of human brain tumors – A review," *Journal of Biomedical Photonics & Engineering* **6**(2), 3375 (2020).
29. S. Oh, S.-H. Kim, Y. Ji, K. Jeong, Y. Park, J. Yang, D. Park, S. Noh, S.-G. Kang, Y.-M. Huh, J.-H. Son, and J.-S. Suh, "Study of freshly excised brain tissues using terahertz imaging," *Biomed. Opt. Express* **5**(8), 2837–2842 (2014).
30. Y. Zou, J. Li, Y. Cui, P. Tang, L. Du, T. Chen, K. Meng, Q. Liu, H. Feng, J. Zhao, M. Chen, and L. Zhu, "Terahertz spectroscopic diagnosis of myelin deficit brain in mice and rhesus monkey with chemometric techniques," *Sci. Rep.* **7**(1), 5176 (2017).
31. K. Meng, T.-N. Chen, T. Chen, L.-G. Zhu, Q. Liu, Z. Li, F. Li, S.-C. Zhong, Z.-R. Li, H. Feng, and J.-H. Zhao, "Terahertz pulsed spectroscopy of paraffin-embedded brain glioma," *J. Biomed. Opt.* **19**(7), 077001 (2014).
32. S. Yamaguchi, Y. Fukushi, O. Kubota, T. Itsuji, T. Ouchi, and S. Yamamoto, "Origin and quantification of differences between normal and tumor tissues observed by terahertz spectroscopy," *Phys. Med. Biol.* **61**(18), 6808–6820 (2016).
33. S. Yamaguchi, Y. Fukushi, O. Kubota, T. Itsuji, T. Ouchi, and S. Yamamoto, "Brain tumor imaging of rat fresh tissue using terahertz spectroscopy," *Sci. Rep.* **6**(1), 30124 (2016).
34. Y. Ji, S. Oh, S. Kang, J. Heo, S. Kim, Y. Choi, S. Song, H. Son, S. Kim, J. Lee, S. Haam, Y. Huh, J. Chang, C. Joo, and J. Suh, "Terahertz reflectometry imaging for low and high grade gliomas," *Sci. Rep.* **6**(1), 36040 (2016).
35. L. Wu, D. Xu, Y. Wang, B. Liao, Z. Jiang, L. Zhao, Z. Sun, N. Wu, T. Chen, H. Feng, and J. Yao, "Study of in vivo brain glioma in a mouse model using continuous-wave terahertz reflection imaging," *Biomed. Opt. Express* **10**(8), 3953–3962 (2019).
36. A. Gavdush, N. Chernomyrdin, K. Malakhov, S.-I. Beshplav, I. Dolganova, A. Kosyrkova, P. Nikitin, G. Musina, G. Katyba, I. Reshetov, O. Cherkasova, G. Komandin, V. Karasik, A. Potapov, V. Tuchin, and K. Zaytsev, "Terahertz spectroscopy of gelatin-embedded human brain gliomas of different grades: A road toward intraoperative THz diagnosis," *J. Biomed. Opt.* **24**(02), 1 (2019).
37. N. Chernomyrdin, A. Gavdush, S.-I. Beshplav, K. Malakhov, A. Kucheryavenko, G. Katyba, I. Dolganova, S. Goryaynov, V. Karasik, I. Spektor, V. Kurlov, S. Yurchenko, G. Komandin, A. Potapov, V. Tuchin, and K. Zaytsev, "In vitro terahertz spectroscopy of gelatin-embedded human brain tumors: a pilot study," *Proc. SPIE* **10716**, 107160S (2018).
38. S. Fan, B. Ung, E. Parrott, and E. Pickwell-MacPherson, "Gelatin embedding: a novel way to preserve biological samples for terahertz imaging and spectroscopy," *Phys. Med. Biol.* **60**(7), 2703–2713 (2015).
39. H. Zhao, Y. Wang, L. Chen, J. Shi, K. Ma, L. Tang, D. Xu, J. Yao, H. Feng, and T. Chen, "High-sensitivity terahertz imaging of traumatic brain injury in a rat model," *J. Biomed. Opt.* **23**(03), 1–7 (2018).
40. J. Shi, Y. Wang, T. Chen, D. Xu, H. Zhao, L. Chen, C. Yan, L. Tang, Y. He, H. Feng, and J. Yao, "Automatic evaluation of traumatic brain injury based on terahertz imaging with machine learning," *Opt. Express* **26**(5), 6371–6381 (2018).
41. G. Katyba, K. Zaytsev, N. Chernomyrdin, I. Shikunova, G. Komandin, V. Anzin, S. Lebedev, I. Spektor, V. Karasik, S. Yurchenko, I. Reshetov, V. Kurlov, and M. Skorobogatiy, "Sapphire photonic crystal waveguides for terahertz sensing in aggressive environments," *Adv. Opt. Mater.* **6**(22), 1800573 (2018).
42. E. Pickwell, B. Cole, A. Fitzgerald, V. Wallace, and M. Pepper, "Simulation of terahertz pulse propagation in biological systems," *Appl. Phys. Lett.* **84**(12), 2190–2192 (2004).
43. E. Pickwell, A. Fitzgerald, B. Cole, P. Taday, R. Pye, T. Ha, M. Pepper, and V. Wallace, "Simulating the response of terahertz radiation to basal cell carcinoma using ex vivo spectroscopy measurements," *J. Biomed. Opt.* **10**(6), 064021 (2005).
44. E. Buixaderas, S. Kamba, and J. Petzelt, "Lattice dynamics and central-mode phenomena in the dielectric response of ferroelectrics and related materials," *Ferroelectrics* **308**(1), 131–192 (2004).
45. G. Komandin, V. Nozdrin, A. Gavdush, A. Pronin, O. Porodinkov, I. Spektor, V. Sigaev, A. Mikhailov, G. Shakhgildyan, V. Ulitko, and D. Abdullaev, "Effect of moisture adsorption on the broadband dielectric response of SiO₂-based nanoporous glass," *J. Appl. Phys.* **126**(22), 224303 (2019).
46. Y. Onodera, "Breakdown of Debye's model for dielectric relaxation in high frequencies," *J. Phys. Soc. Jpn.* **62**(11), 4104–4107 (1993).
47. P. Martin, "Sum rules, Kramers-Kronig relations, and transport coefficients in charged systems," *Phys. Rev.* **161**(1), 143–155 (1967).
48. K. Cole and R. Cole, "Dispersion and absorption in dielectrics I. alternating current characteristics," *J. Chem. Phys.* **9**(4), 341–351 (1941).
49. K. Cole and R. Cole, "Dispersion and absorption in dielectrics II. direct current characteristics," *J. Chem. Phys.* **10**(2), 98–105 (1942).
50. D. Davidson, "Dielectric relaxation in liquids: I. The representation of relaxation behavior," *Can. J. Chem.* **39**(3), 571–594 (1961).
51. S. Havriliak and S. Negami, "A complex plane analysis of α -dispersions in some polymer systems," *J. Polym. Sci. Part C: Polym. Symp.* **14**(1), 99–117 (2007).
52. P. Wesseling and D. Capper, "WHO 2016 classification of gliomas," *Neuropathol. Appl. Neurobiol.* **44**(2), 139–150 (2018).
53. J. Jeong, C. Juhász, S. Mittal, E. Bosnyak, D. Kamson, G. Barger, N. Robinette, W. Kupsky, and D. Chugani, "Multi-modal imaging of tumor cellularity and tryptophan metabolism in human gliomas," *Cancer Imag.* **15**(1), 10 (2015).

54. O. Cherkasova, M. Nazarov, M. Konnikova, and A. Shkurinov, "THz spectroscopy of bound water in glucose: direct measurements from crystalline to dissolved state," *J. Infrared, Millimeter, Terahertz Waves* **41**(9), 1057–1068 (2020).
55. S. Yurchenko and K. Zaytsev, "Spectroscopy of Nafion in terahertz frequency range," *J. Appl. Phys.* **116**(11), 113508 (2014).
56. G. Komandin, S. Chuchupal, S. Lebedev, Y. Goncharov, A. Korolev, O. Porodinkov, I. Spektor, and A. Volkov, "BWO generators for terahertz dielectric measurements," *IEEE Trans. THz Sci. Technol.* **3**(4), 440–444 (2013).
57. A. Sdobnov, M. Darvin, J. Schleusener, J. Lademann, and V. Tuchin, "Hydrogen bound water profiles in the skin influenced by optical clearing molecular agents – Quantitative analysis using confocal Raman microscopy," *J. Biophotonics* **12**(5), e201800283 (2019).
58. B. Truong, H. Tuan, V. Wallace, A. Fitzgerald, and H. T. Nguyen, "The potential of the double Debye parameters to discriminate between basal cell carcinoma and normal skin," *IEEE Trans. THz Sci. Technol.* **5**(6), 990–998 (2015).
59. X. Chen, Q. Sun, J. Wang, H. Lindley-Hatcher, and E. Pickwell-MacPherson, "Exploiting complementary terahertz ellipsometry configurations to probe the hydration and cellular structure of skin in vivo," *Advanced Photonics Research*, Accepted (2020), <https://doi.org/10.1002/adpr.202000024>.
60. A. Bashkatov, K. Berezin, K. Dvoretzkiy, M. Chernavina, E. Genina, V. Genin, V. Kochubey, E. Lazareva, A. Pravdin, M. Shvachkina, P. Timoshina, D. Tuchina, D. Yakovlev, D. Yakovlev, I. Yanina, O. Zhernovaya, and V. Tuchin, "Measurement of tissue optical properties in the context of tissue optical clearing," *J. Biomed. Opt.* **23**(09), 091416 (2018).
61. N. Chernomyrdin, A. Lesnichaya, E. Yakovlev, K. Kudrin, O. Cherkasova, E. Rims kaya, V. Kurlov, V. Karasik, I. Reshetov, V. Tuchin, and K. Zaytsev, "Differentiation of basal cell carcinoma and healthy skin using multispectral modulation autofluorescence imaging: A pilot study," *J. Biomed. Photonics Eng.* **5**(1), 010302 (2019).
62. Z. Abbas, V. Gras, K. Möllenhoff, A.-M. Oros-Peusquens, and N. Shah, "Quantitative water content mapping at clinically relevant field strengths: A comparative study at 1.5T and 3T," *NeuroImage* **106**, 404–413 (2015).
63. H. Neeb, K. Zilles, and N. Shah, "A new method for fast quantitative mapping of absolute water content in vivo," *NeuroImage* **31**(3), 1156–1168 (2006).
64. H. Neeb, V. Ermer, T. Stocker, and N. Shah, "Fast quantitative mapping of absolute water content with full brain coverage," *NeuroImage* **42**(3), 1094–1109 (2008).
65. G. DiResta, J. Lee, and E. Arbit, "Measurement of brain tissue specific gravity using pycnometry," *J. Neurosci. Methods* **39**(3), 245–251 (1991).
66. E. Yakovlev, K. Zaytsev, I. Dolganova, and S. Yurchenko, "Non-destructive evaluation of polymer composite materials at the manufacturing stage using terahertz pulsed spectroscopy," *IEEE Trans. THz Sci. Technol.* **5**(5), 810–816 (2015).
67. W. Yager, "The distribution of relaxation times in typical dielectrics," *Physics* **7**(12), 434–450 (1936).
68. J. Liu, X. He, J. Zhang, and L.-W. Qi, "Hydrogen-bond structure dynamics in bulk water: insights from ab initio simulations with coupled cluster theory," *Chem. Sci.* **9**(8), 2065–2073 (2018).
69. C. Joseph, R. Patel, V. Neel, R. Giles, and A. Yaroslavsky, "Imaging of ex vivo nonmelanoma skin cancers in the optical and terahertz spectral regions optical and terahertz skin cancers imaging," *J. Biophotonics* **7**(5), 295–303 (2014).
70. N. Chernomyrdin, A. Kucheryavenko, G. Kolontaeva, G. Katyba, I. Dolganova, P. Karalkin, D. Ponomarev, V. Kurlov, I. Reshetov, M. Skorobogatiy, V. Tuchin, and K. Zaytsev, "Reflection-mode continuous-wave 0.15- λ -resolution terahertz solid immersion microscopy of soft biological tissues," *Appl. Phys. Lett.* **113**(11), 111102 (2018).
71. N. Chernomyrdin, A. Kucheryavenko, E. Rims kaya, I. Dolganova, V. Zhelnov, P. Karalkin, A. Gryadunova, I. Reshetov, D. Lavrukhin, D. Ponomarev, V. Karasik, and K. Zaytsev, "Terahertz microscope based on solid immersion effect for imaging of biological tissues," *Opt. Spectrosc.* **126**(5), 560–567 (2019).